Mean transverse energy, surface chemical and physical characterization of CERN-made Cs-Te photocathodes

L. B. Jones[1,2,*] H. Panuganti[3,†] C. Benjamin[1,4] E. Chevallay[3] H. M. Churn[1,2]
V. Fedosseev[3] T. C. Q. Noakes[1,2] L. A. J. Soomary[2,5] and C. P. Welsch[2,5]

[1]*Accelerator Science and Technology Centre, STFC Daresbury Laboratory,
Warrington WA4 4AD, United Kingdom*
[2]*The Cockcroft Institute of Accelerator Science, Warrington WA4 4AD, United Kingdom*
[3]*The European Organization for Nuclear Research (CERN), 1211 Geneva 23, Switzerland*
[4]*Department of Physics, University of Warwick, Coventry CV4 7AL, United Kingdom*
[5]*Department of Physics, University of Liverpool, Liverpool L69 7ZE, United Kingdom*

Cesium telluride photocathodes are known to offer high quantum efficiencies under UV illumination combined with good lifetimes compared to other semiconductor photocathodes, making them very popular electron sources for particle accelerator applications. The development of photocathode preparation, characterization, and related expertise at a single accelerator laboratory can be challenging, expensive, and time consuming. Recognizing this, we explored the use of a custom-designed ultrahigh vacuum suitcase for transportation of CERN-made (Switzerland) cesium telluride photocathodes to Daresbury Laboratory (UK) for characterization. We report the synthesis and characterization of a batch of four cesium telluride photocathodes corresponding to our second attempt of transport, following design and process improvements through lessons learned from our first attempt. The photocathode characterization involved, where possible, measurements of the surface elemental composition using x-ray photoelectron spectroscopy (XPS), surface roughness with an in-vacuum scanning tunneling microscope (STM), and quantum efficiency (QE) measurements. Transverse energy distribution curves were obtained over a wide range of illumination wavelengths using the transverse energy spread spectrometer (TESS) at room- and cryogenic temperatures, and the values for mean transverse energy (MTE) were extracted. The photocathodes exhibited distinct thicknesses ranging from ~50 to ~120 nm and significant MTE beyond the photoemission threshold which is attributed to the presence of Cs_xO and Cs phases, as confirmed by XPS analysis. The photocathode that exhibited no carbon or oxygen contamination was measured to have the highest QE of 2.9% at a wavelength of 265 nm at the end of the performance characterization process. The results presented herein offer an insight into the achievements possible through international collaborations by successfully utilizing long-distance transportation of photocathodes by land under ultrahigh vacuum conditions.

I. INTRODUCTION

Semiconductor photocathodes are widely used as electron beam sources in particle accelerators owing to their high quantum efficiency (QE) when compared to metallic photocathodes [1], despite their more stringent requirements for ultrahigh vacuum (UHV). Cesium telluride (Cs-Te) photocathodes are popular and practical in the positive electron affinity semiconductor class since they offer nominal QEs up to 20% [2–4], subpicosecond response times [5,6], and relatively long operational lifetimes in comparison to the negative electron affinity class. The intrinsic emittance (ϵ_i) of a photocathode is closely related to its mean transverse energy (MTE) and is a crucially important figure of merit related to electron beam quality at the point of generation. The MTE is progressively reduced as the illumination wavelength is increased, reaching its minimum defined by the thermal floor (k_BT, where k_B is the Boltzmann constant and T is the temperature) at the photoemission threshold [7]. Besides increasing the brightness, emittance reduction can decrease the physical footprint of an accelerator and thus could reduce the cost and complexity of apparatus and operations [8]. High-brightness electron beams with low emittance are critical

---

*Corresponding author: lee.jones@stfc.ac.uk
†Corresponding author: harsha.panuganti@cern.ch

for advanced accelerators like energy recovery linacs (ERLs) [9], free electron lasers (FELs) [10,11], and future lepton colliders [12].

Practically, ϵ_i is dependent on the photocathode synthesis process which affects the photocathode physical and chemical characteristics like surface topography, stoichiometry, and work function (ϕ). Measurements of these characteristics are crucial to analyze and improve the substrate preparation and synthesis processes. However, these measurements require effective transfer and transport of Cs-Te photocathodes in UHV conditions from the preparation chamber to and from the respective measurement apparatus. Moreover, the development of such comprehensive expertise and instrumentation for both synthesis and extensive characterization can be difficult and expensive to establish at any single accelerator facility.

CERN's photoemission laboratory has routinely produced Cs-Te photocathodes over the last three decades and has supported CERN's experiments and programs such as the proposed Compact Linear Collider (CLIC) [13], CERN Linear Electron Accelerator for Research (CLEAR) [14], and the Advanced Proton Driven Plasma Wakefield Acceleration (AWAKE) [15]. The focus for these programs has generally been on achieving a specific bunch charge, with beam emittance considered as a secondary priority. Consequently, facilities to measure photocathode MTE and surface roughness in order to minimize intrinsic emittance have not been established at CERN. The Science and Technology Facilities Council (STFC), Daresbury Laboratory, has been developing expertise and facilities for characterization and optimization of photocathodes for more than a decade and can provide the aforementioned insights needed by CERN. The emittance (ϵ) requirements for run 2 of the AWAKE experiment [16] are much more stringent ($\epsilon = 2$ μm; see Table 1 in Ref. [17] for additional beam parameter requirements) than those for CLIC and CLEAR. Consequently, a CERN–STFC collaboration to carry out the characterization of CERN's Cs-Te photocathodes is a sensible step to optimize photocathode performance for CERN's electron accelerators. There have been similar successful collaborations involving long-distance transportation of photocathodes from the INFN laboratory in Italy to DESY [18,19] and PITZ [19,20] in Germany, and to FAST and APEX [21,22] in the United States. The motivation in this instance was to utilize capabilities not available at CERN.

The photocathode research and development facilities at Daresbury Laboratory include several systems: a III–V Photocathode Preparation Facility (PPF) for GaAs [23] originally constructed for the Accelerators and Lasers in Combined Experiments (ALICE) ERL [24]; the "Multiprobe" surface analysis chamber which provides x-ray photoelectron spectroscopy (XPS) to characterize

surface chemistry, and atomic force microscopy (AFM) and scanning tunnelling microscopy (STM) for surface roughness measurements, and a laser system for QE measurements at 266 nm laser wavelength [25]; and most notably, the transverse energy spread spectrometer (TESS) to measure MTE (and QE) [26]. Building on this collaboration experience with CERN's photoemission laboratory, Daresbury Laboratory is currently developing an Alkali Photocathode Preparation Facility [27] which is intended to provide Cs-Te photocathodes for the Compact Linear Accelerator for Research Applications (CLARA) [28] allowing for significantly higher QEs than those of the metal (polycrystalline copper) photocathodes currently in use. Cs-Te photocathodes would potentially benefit work on very high energy electron energy (VHEE) FLASH radiotherapy that requires CLARA to deliver high bunch charges in the nC range to achieve dose rates in excess of 40 Gy/s [29]. Additionally, experiments on novel acceleration techniques such as THz, dielectric, and plasma wakefield acceleration schemes [30] require electron bunches with charges >1 nC which are enabled by Cs-Te photocathodes.

The goal of the current research collaboration was to synthesize a batch of four Cs-Te photocathodes at CERN's photoemission laboratory using a well-established co-deposition method and transport them overland to Daresbury Laboratory in a dedicated motor vehicle using a custom-designed UHV suitcase for surface physical and chemical characterization. In the current manuscript, we report the synthesis and characterization of Cs-Te photocathodes transported as a part of our phase II (second attempt) research, after making improvements to the apparatus design and processes from the lessons learned in our phase I trial (first attempt) whose results are detailed in Ref. [31]. The improvements made in the phase II research compared to the phase I trial include (i) improvement in substrate preparation and mounting, (ii) improvement in elemental deposition process controls of photocathode synthesis, (iii) improved design and increased vacuum pumping capacity of the UHV suitcase, (iv) inclusion of pressure logging device in the suitcase for estimation of gas exposure (dose) to photocathodes during transportation.

The photocathode characterization in phase II involved measurements of MTE using the TESS at room- and cryogenic temperatures, supported by surface stoichiometry estimation involving XPS, surface roughness using an in-vacuum STM, and QE using the Multiprobe system.

Section II describes the substrate preparation, the photocathode preparation chamber, and the synthesis method. Section III details the vacuum suitcase design and performance. Section IV discusses the MTE analysis and relative QE measurements. Section V discusses the surface topography and surface roughness measurements using STM. Section VI presents the XPS analysis. Section VII presents

absolute QE measurements. Section VIII summarizes and discusses our results. Finally, Sec. IX concludes this research work with a future outlook.

II. PHOTOCATHODE SYNTHESIS

The photocathode synthesis began with substrate preparation. Surface Preparation Laboratories B.V. supplied Daresbury Laboratory with four polycrystalline copper substrate pucks of diameter 6 mm. On receipt, the pucks were cleaned in acetone in an ultrasonic bath and then mounted in cathode holders based on the Scienta Omicron 19 mm flag system [32]. These were then loaded into the Multiprobe system where they were treated to repeated cycles of argon ion bombardment (15 min) and annealing at 550 °C (60 min) until clean XPS spectra were measured. Once atomically clean XPS spectra were obtained, mean surface roughness (R_a) was measured using an Omicron AFM/STM.

The surface roughness measurements confirmed that the clean pucks exceeded the roughness specification of $R_a < 30$ nm, with $5 < R_a < 10$ nm measured for all of the pucks. The four mounted bare pucks were then transferred into the vacuum suitcase (see Fig. 5). Once loaded, the suitcase was sealed and dismounted from the Multiprobe, then placed into its transit crate for overland transportation to CERN, maintaining UHV conditions throughout (see Sec. III).

CERN's photoemission laboratory uses a co-deposition process to synthesize Cs-Te photocathodes. Co-deposition methods are known to yield more photosensitive photocathodes when compared to sequential deposition methods [33–35], one possible factor being reduced contamination from residual gases [36]. The photocathode preparation chamber houses up to two wire-shaped Cs dispensers (SAES Getters S.p.S) that consist of Cs chromate with Zr-Al (St 101 alloy) reducing agents and a homemade Te dispenser. The Te dispenser is based on a molybdenum crucible containing pure Te with impurities $\leq 1 \times 10^{-4}\%$. When heated to the correct temperatures, the dispensers release pure vapors of the corresponding elements. The deposition rates are independently controlled by their respective dispenser power supplies, via resistive heating. A pair of quartz microbalances monitor the deposition thickness of Cs and Te separately. When not in operation, the preparation chamber is typically maintained at a pressure $\leq 4 \times 10^{-11}$ mbar. Depending on the dispenser temperatures, the pressure in the preparation chamber could rise up to 5×10^{-7} mbar during the deposition process. A frequency upconverted commercial flash-lamp pumped Q-switched Nd:YAG laser system (Spectron SL802) provides 266 nm laser pulses at a 10 Hz repetition rate. The laser beam is delivered to the center of the photocathode through a series of mirrors. For QE optimization during deposition, the generated photocurrent can be monitored in real time by means of a circular anode biased at 1 kV potential with

respect to the cathode. The deposition process can be stopped by means of a mechanical shutter that quickly shields the photocathode surface from deposition. A residual gas analyzer system is installed in the preparation chamber in order to monitor for any gaseous contaminants. CERN's photoemission laboratory's apparatus and methods are described in more detail in Refs. [37,38].

A batch of four Cs-Te photocathodes, viz., cathodes P5 → P8 (cathodes P1 → P4 correspond to the phase I trial [31]), were synthesized on four different days. Each substrate puck was extracted from the vacuum suitcase and transferred into the photocathode preparation chamber for the Cs-Te deposition process and then transferred back into the suitcase. The pucks were exposed to the atmosphere during the recommissioning of the preparation chamber before photocathode deposition, but they remained in UHV after the deposition. Loading substrates from the atmosphere matches CERN's standard procedure for the deposition of Cs-Te photocathodes and therefore makes this work a better comparison with previous results [39]. For each photocathode, the deposition process started with stabilizing Te deposition rate to ~0.1 nm/ min before introducing the Cs vapor. The Cs and Te deposition rates were gradually increased by the operator to maximize the photocurrent, by controlling the respective dispenser
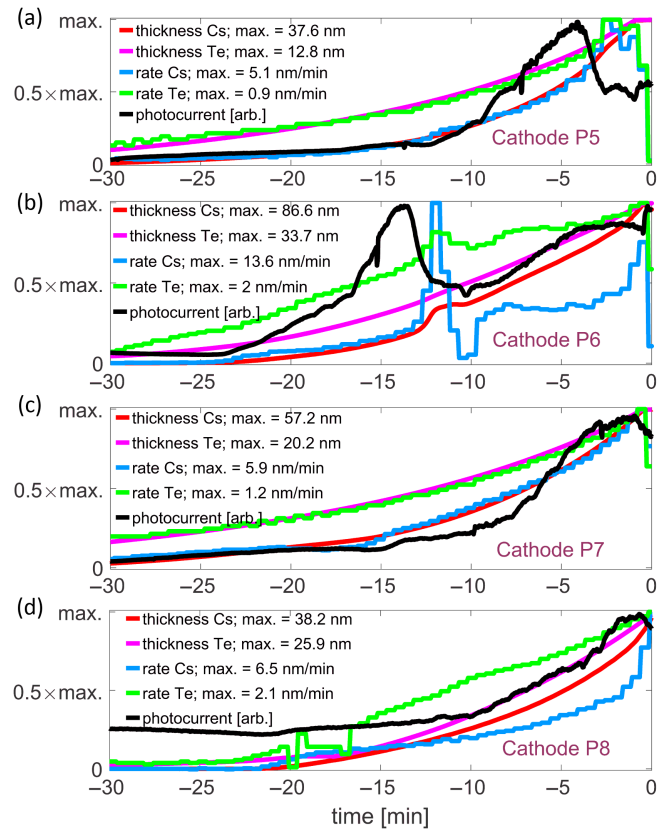
FIG. 1. Critical deposition parameters and photocurrent recorded during the synthesis of cathodes P5(a) → P8(d).

TABLE I. Final elemental deposition thickness values for each photocathode. The Cs:Te overall deposition ratio is shown for reference, which may not directly correlate to the elemental ratio on the surface as per XPS analysis.

Photocathode thickness (nm)	Cs thickness	Te thickness	Cs:Te deposition ratio
P5 (50.4)	37.6	12.8	2.9 : 1
P6 (120.3)	86.6	33.7	2.6 : 1
P7 (77.4)	57.2	20.2	2.8 : 1
P8 (64.1)	38.2	25.9	1.5 : 1

currents. The deposition was stopped using the shutter when the photocurrent appeared to not improve despite deposition rate adjustments.

The synthesis parameters for each photocathode were recorded in real time at a data acquisition rate of 2 Hz. The corresponding data relating to Cs and Te deposition rate and thickness and photocurrent are displayed in Fig. 1. The elemental deposition rates were numerically computed based on the thickness values. For better visualization and without loss of validity, a ten-point moving average was applied to the deposition rate and photocurrent curves in the plots. Only the critical and final 30 min of deposition parameters are displayed in Fig. 1, where the time value "0" corresponds to the end of the deposition. Since the deposition rates are adjusted manually to maximize the photocurrent, each photocathode may exhibit different thickness and QE subjected to the operator's judgment regarding when the deposition process should be terminated. The notably high photocurrent baseline for cathode P8 in Fig. 1(d) is attributed to spurious electron emission from other coated surfaces. Over time, such spurious emission is overridden by the real photocurrent from the photocathode. Therefore, spurious emission does not significantly affect photocurrent optimization.

The final elemental thickness values recorded for each photocathode are summarized in Table I. The substrate temperature for each photocathode is simply the ambient temperature that day; no substrate heating was used.

III. PHOTOCATHODE TRANSPORT

A. UHV suitcase design

The design objective for the UHV suitcase was to securely accommodate up to four cathode holders in a magazine and allow for the transfer of each cathode holder to and from CERN's photocathode preparation chamber [38] via a transfer-arm assembly, to maintain UHV conditions during transportation to Daresbury, and ultimately to allow cathode transfer into the TESS and Multiprobe photocathode characterization facilities. To maintain compatibility with the CERN preparation chamber, an adapter shown in Fig. 5 based on the CERN photocathode puck

was installed into the preparation chamber which accepted the Omicron 19 mm flag sample holders.

The vacuum suitcase was developed progressively based on extensive testing during phase I and phase II trials of the research. The final version of the UHV suitcase consists of a four-way cross that connects to the transfer-arm assembly via an all-metal gate valve, as shown in Fig. 5. The suitcase comprises a magnetically coupled translation arm to translate the cathode holder magazine, an ion pump with integrated NEG pump, and an additional NEG cartridge (SAES Getters CapciTorr D 50) which was added to the suitcase for the return trip; see Fig. 5. The ion pump was driven by a battery-powered supply (Ferrovac LSA2.1) which was backed up by a 12 V, 95 A.h, 850 A lead-acid automobile battery. The transfer of a given cathode holder was achieved by first aligning the given cathode holder in the magazine to the transfer arm in both rotation and position, then gripping the sample holder tongue via an Omicron tong mechanism [40] built into the arm. The transfer arm allows for the transfer of a cathode holder into the CERN cathode plug adapter or other vacuum systems.

Pressure logging was achieved by recording a voltage analog of the current through the ion pump driver via the external voltage–current data logger (Chauvin Arnoux L452), and using an appropriate calibration factor to convert voltage to suitcase pressure.

B. UHV suitcase performance

Figure 2(a) shows the pressure profile and the corresponding residual gas dose delivered (Langmuir [L]) to the substrate pucks during the overland transit of the suitcase from Daresbury Laboratory to CERN as a test run. In order to minimize mechanical jerks during the transit, the suitcase was transported on a dedicated commercial vehicle with air-cushioned suspension. Figure 2(b) shows the pressure and integrated gas dose delivered to the finished photocathodes during their transit from CERN to Daresbury Laboratory; these return transport data correspond to a longer time of transit due to logistical delays. The pressure spikes in the figure correspond to the mechanical jerks caused during the transport while the flat regions correspond to stops and periods of rest.

It should be noted that Fig. 2(a) corresponds to the absence of the NEG cartridge; the improvement in vacuum sustenance in Fig. 2(b) is attributed to the addition of the D 50 NEG cartridge. The plots in Fig. 2 had negative pressure (voltage) values as recorded by the data logger, whose source of origin has not been identified. These negative values have been forced to zero in the figure, assumed to be spurious, as they do not correspond to a real case. Therefore, the pressure and gas dose data shown in Fig. 2 represent the optimistic case, contrary to incorporating a positive pressure offset to compensate for the negative values, for instance.
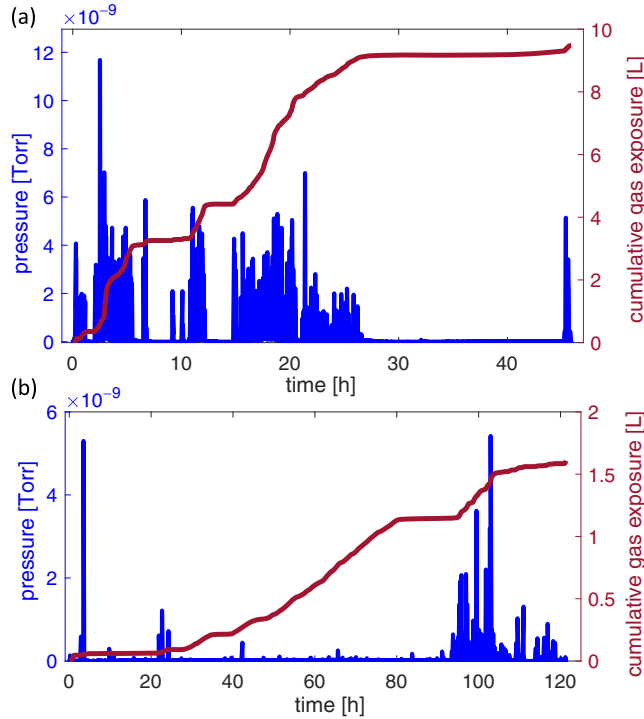
FIG. 2. Pressure profile inside the UHV suitcase and the corresponding gas dose delivered as a function of time, during transport from Daresbury Laboratory to CERN (loaded with substrate pucks) (a) and from CERN to Daresbury Laboratory (loaded with finished photocathodes) (b).

FIG. 3. Photographs acquired under the same lighting and camera conditions of the four Cs-Te photocathodes as received at Daresbury Laboratory during their transfer from the vacuum suitcase into the PPF storage carousel.

A previous study [41] where a controlled exposure of oxygen to a Cs-Te photocathode resulted in the decrease of QE ($\lambda = 254$ nm) from 5.1% to 3.1% for a dose of 26.5 L. In comparison, the UHV suitcase delivered a gas dose of 1.6 L [Fig. 2(b)] of unknown gas (presumably less reactive than pure oxygen) to the photocathodes during transport. This validates the UHV design and performance of the suitcase in terms of the gas dose delivered, although QE measurements of the photocathodes before and after the UHV transport (not made) would be desirable to further confirm and quantify this point.

IV. PHOTOEMISSION CHARACTERIZATION

On its return to the STFC Daresbury Laboratory, the vacuum suitcase was immediately connected to the PPF loading chamber [23]. The photocathodes were sequentially extracted from the suitcase under vacuum and photographed *in situ* (as shown in Fig. 3) before being moved onto the GaAs photocathode storage carousel as the vacuum level in this chamber is excellent with a base pressure of 3×10^{-12} mbar. The cathodes were characterized in the order P5, P7, P8, and P6, first for photoemission properties using the TESS, and then for surface and chemical properties using the Multiprobe.

A. Mean transverse energy

The photoemission characteristics for each photocathode were measured using the TESS following the processes outlined in our previous publications [26,42] describing the operation of the TESS, photoemission data acquisition, and subsequent analysis. Transverse energy distribution curves (TEDC) were obtained for all photocathodes under a wide range of illumination wavelengths, beginning at 236 nm where photoemission was strong and moving in 10 nm steps to some point beyond their photoemission threshold. These measurements were carried out at room temperature ($\sim$298 K) and under cryogenic conditions ($\sim$190 K) with each photocathode cooled with N_2 gas passed through a liquid nitrogen cooling loop. Single values for the MTE at each illumination wavelength were extracted from the TEDCs using Eq. (1) where ε_{tr} is the electron transverse energy and $N_e(\varepsilon_{tr})$ is the function describing the numeric distribution of electron transverse energies:

$$\text{MTE}[N_e(\varepsilon_{tr})] = \frac{\int_0^\infty \varepsilon_{tr} \cdot N_e(\varepsilon_{tr}) d\varepsilon_{tr}}{\int_0^\infty N_e(\varepsilon_{tr}) d\varepsilon_{tr}}. \quad (1)$$

This single value for MTE is a crucial performance metric as it couples directly into the photocathode intrinsic emittance (ϵ_i) derived initially in Ref. [43] and developed further in Ref. [7]:

$$\epsilon_i = \sigma_x \sqrt{\frac{\hbar\omega - \phi_{\text{eff}}}{3m_e c^2}} = \sigma_x \sqrt{\frac{\text{MTE}}{m_e c^2}}, \quad (2)$$
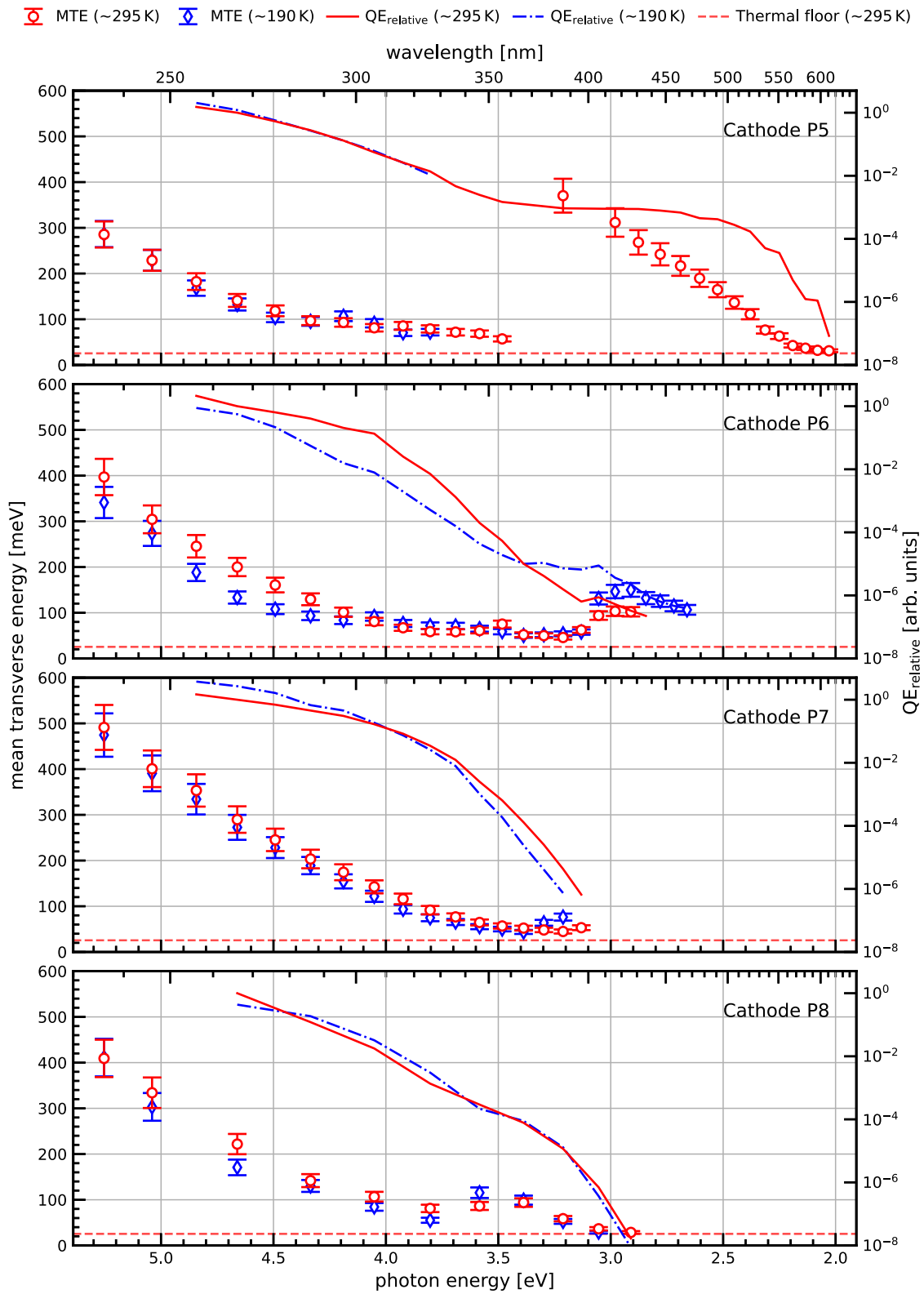
FIG. 4.   Summary of cryogenic and room temperature MTE measurements for Cathodes P5 → P8.

where σ_x is the rms emission area on the photocathode surface, m_e is the electron mass, and c the speed of light. It can be seen that reducing MTE also reduces the source intrinsic emittance. Our MTE results are summarized in Fig. 4, and they are discussed in detail in Sec. VIII with the qualitative response linked to their respective surface composition.

B. Relative quantum efficiency

Photoemission image data obtained from the TESS were also used to estimate the QE for each photocathode and permit relative comparisons over a range of illumination wavelengths. This was accomplished by combining the illumination intensity (optical power) with the detector chain settings to assess the overall gain in the TESS measurement and then using this to normalize the integrated photoemission footprint. In a characterization measurement, the gain provided by the TESS detector MCP (microchannel plate) was found to double for each 41.0 ± 0.4 V increase in the potential difference between the MCP front and MCP back over the typical voltage range applied to the MCP during TEDC measurements [26]. We can therefore estimate the MCP gain (G_{mcp}) over this region using

$$G_{\mathrm{mcp}} = 2^{\left(\frac{\Delta V_{\mathrm{mcp}}}{41.0}\right)}, \qquad (3)$$

where ΔV_{mcp} is the voltage difference between the MCP back and front plates. The relative quantum efficiency (QE_{relative}) is then calculated using Eq. (4):

$$QE_{\mathrm{relative}} = \frac{I_{\mathrm{corrected}} \times hc}{t \cdot (P_{\mathrm{opt}} \times \lambda \times T_{\mathrm{viewport}}) \cdot G_{\mathrm{mcp}}}, \qquad (4)$$

where $I_{\mathrm{corrected}}$ is the total photoemission image intensity following correction by subtraction of the dark image, h is Planck's constant, t is the data acquisition exposure time, P_{opt} is the optical power measured immediately before the sapphire viewport into the TESS vacuum chamber, λ the illumination wavelength and T_{viewport} is the wavelength-dependent transmission through the uncoated sapphire viewport.

This approach does not yield an absolute value for QE at any specific wavelength, but it is a useful mechanism for making meaningful comparisons of the photoemissive output of different cathodes at different wavelengths.

The relative QE data shown in Fig. 4 have been normalized to the 266 nm value at room temperature. The data corresponding to cryogenic temperatures have been scaled accordingly to preserve the relative differences.

V. SURFACE PHYSICAL ANALYSIS (STM)

Surface roughness was measured for the P5, P7, and P8 cathodes by STM using the Omicron AFM/STM in the Multiprobe. Three positions were investigated, with position 1 being the photocathode geometric center, position 2

TABLE II. STM surface roughness measurements covering a 500×500 nm^2 area for the P5–P8 photocathodes.

Cathode	Position	rms, R_q (nm)	Mean, R_a (nm)
P5	1	6.1	4.5
	2	12.3	10.5
	3	11.1	9.0
P6	⋯	⋯	⋯
P7	1	11.1	8.8
	2	8.1	6.8
	3	5.4	4.2
P8	1	5.0	4.1

having a radial displacement of ∼0.75 mm, and position 3 the largest possible radial displacement of the STM tip from the center, ∼1.5 mm. The raw data were analyzed using Gwyddion [44] to define a "Plane Level" and then extract values for rms (R_q) and mean (R_a) surface roughness.

Unfortunately, the STM tip broke after the first surface roughness measurement at the center of the P8 photocathode. During replacement of the STM tip, the STM tip holder broke thus rendering the STM system unserviceable. This prevented any further surface roughness measurements on the P8 cathode and prevented us from making any STM measurements whatsoever on the P6 cathode. Table II summarizes the analysis of the surface roughness measurements that were made, and the source images are shown in Fig. 6 in Appendix B. The postdeposition surface roughness data we obtained showed that the level of roughness remains very low, with the measured values of R_a and R_q being similar to those for the bare pucks prior to dispatch from Daresbury Laboratory.

VI. SURFACE CHEMICAL ANALYSIS (XPS)

XPS survey spectra were measured to establish the chemical nature of the photoemissive surface. Cs, Te, and the expected contaminants O and C were the only elements identified in the survey scans, so our attention was then focused on these regions. Spectra were obtained using a non-monochromated Mg K$_\alpha$ x-ray source (1253.6 eV) and a Thermo Alpha 110 hemispherical electron energy analyzer. The analyzer transmission function was determined experimentally using the technique described in Ref. [45], and the effective analyzer work function (4.26 eV) was calibrated using the Ag Fermi edge. Survey and core region spectra were acquired with pass energies of 50 and 20 eV, respectively. XPS data analysis was conducted using the CasaXPS software package with a mix of Gaussian–Lorentzian functions and a standard Shirley background subtraction across all cathodes for all spectra discussed [46]. All reference binding energies used for curve fitting were taken from the NIST X-ray Photoelectron Database [47]. Relative sensitivity factors

TABLE III. Summary of the elemental concentrations for the P6, P7, and P8 photocathodes. Complete XPS data with specific elemental bonding environments are shown in Appendixes C, D, and E, respectively.

Cathode	Elemental concentration (%)			
	Cs	Te	O	C
P6	54.3	35.3	6.2	4.2
P7	54.6	41.9	3.5	
P8	50.9	49.1		

(RSFs) derived from the Scofield cross sections [48] were used to scale the peak areas to facilitate meaningful peak fitting and elemental composition analysis. It is possible that we have overestimated the amount of elemental Te due to the overlap of the Te $3d^{5/2}$ plasmon loss feature with those of the Te $3d^{3/2}$ plasmon loss and the Te $3d^{5/2}$ photoemission features. This was accounted for when fitting the Te $3d$ features by constraining the full width at half maximum (FWHM) and component intensities between the spin orbits.

We have not presented our XPS data for the P5 photocathode as this was dropped inside the TESS following the completion of TEDC data acquisition, and its recovery necessitated the venting of the system and therefore its exposure to atmospheric contamination. Detailed XPS data for the P6, P7, and P8 photocathodes and the assigned chemical bonding environments can be found in Appendixes C, D, and E, respectively, while Table III summarizes the elemental composition of each cathode.

Cathode P6: The XPS spectra in Fig. 7 in Appendix C show an elemental ratio of Cs:Te to be 1.5:1 and a small presence of contamination in the form of oxygen and carbon with atomic percentages of 6.2% and 4.2%, respectively. The Te core region spectra have one distinguishable peak for each spin orbit at binding energies of 572.3 and 582.7 eV for the Te $3d^{5/2}$ and Te $3d^{3/2}$, respectively. This is a shift of -0.7 eV from the reference binding energy of elemental Te [47]. Previous XPS studies on Cs_2Te in Ref. [49] show binding energies of 571.1 and 581.5 eV for $3d^{5/2}$ and $3d^{3/2}$, respectively. The observed smaller shift in our spectra suggests a different Cs_xTe phase with a reduced Cs concentration compared to Cs_2Te. When considering the contaminants on the surface, the carbon present on the sample has been associated with CO components as they align with binding energies in the O 1s and C 1s spectra. Excess oxygen present is assumed to be associated with Cs oxide due to the lack of Te oxide peaks present in the spectra.

Cathode P7: The XPS spectra in Fig. 8 show the elemental ratio of Cs:Te to be 1.3:1 and that the only contaminant present is oxygen with an atomic concentration of 3.5%. The Te $3d^{5/2}$ features two distinct components whose peak positions strongly suggest Cs_2Te at

571.2 eV and elemental Te at 572.9 eV which closely match previous XPS studies [49]. We assert the O present on the sample is not bound to Te due to the lack of a third peak at around 576.1 or 577.0 eV, so in the absence of Te oxide peaks, we assume that the excess O present is present as a Cs oxide.

Cathode P8: The XPS spectra shown in Fig. 9 in Appendix E suggest a surface elemental Cs:Te ratio of 1:1, with no detectable presence of C or O contamination. However, further analysis of the bonding environment explains the apparently high abundance of Te on the P8 photocathode surface. Similar to P7, two distinct components are observed in the Te $3d^{5/2}$ at binding energies of 571.2 eV which we can associate with Cs_2Te, and at 572.8 eV aligning with elemental Te. Considering the total Cs present and Te which is not in an elemental state, the Cs:Te ratio is 2.6:1 suggesting that excess Cs is present in the sampling region. Due to the following factors such as the reactivity of Cs and its affinity for O, the narrower FWHM used in peak fitting in comparison to those used in the spectra measured for the P6 and P7 cathodes, and the relative abundance of Cs to Te, the Cs is assumed to be fully bonded to Te on the sample and simply fitted with a single component for each spin orbit in the Cs 3d region, as shown in Fig. 9. The lack of oxygen in the P8 spectra further supports the premise that there was no elemental Cs present on this photocathode surface.

VII. QUANTUM EFFICIENCY MEASUREMENT

Table IV summarizes quantum efficiency measurements for the P6–P8 photocathodes. These were carried out in the Multiprobe chamber following the completion of photoemission measurements in the TESS. Those made at 265 nm used a Roithner LaserTeknik DUV-HL5NR LED to illuminate the photocathode while that at 266 nm used a Crylas FQSS 266-Q4 laser.

VIII. RESULTS AND DISCUSSION

A. General trends in MTE and QE

As can be seen in Fig. 4, all of the photocathodes tested exhibited a progressive decrease in their MTE from an initial maximum when illuminated at 236 nm toward the expected thermal floor at the Cs_2Te photoemission threshold which is typically around 350 nm or 3.5 eV [2,33,50].

TABLE IV. Summary of absolute quantum efficiency measurements for the P6 → P8 photocathodes. There is no QE data for the P5 photocathode as it was dropped in the TESS and subsequently exposed to air during its recovery.

Cathode	P6	P7	P8
QE (λ)	0.6% (265 nm)	0.2% (266 nm)	2.9% (265 nm)

However, none of them reached an MTE defined by the thermal floor ($k_B T$), which is 25 meV at room temperature and 16 meV at 190 K. MTEs extracted under cryogenic conditions over this illumination wavelength range were generally below those measured at room temperature due to the narrowing of the Fermi–Dirac electron energy distribution.

The relative QE [see Eq. (4) and Sec. IV B] was not calculated for illumination photon energies above 5.0 eV ($\lambda < 256$ nm) as the optical power in this regime was too low for accurate measurement. Under illumination at photon energies between 5.0 and 3.5 eV ($256 < \lambda < 350$ nm), the relative QE can be seen to decline progressively, as is expected. At the Cs_2Te threshold emission region, the TEDC data from TESS indicate relative QE values in the 10^{-3} to 10^{-4} regime, which is in good agreement with data published in Ref. [2]. As the illumination photon energy is decreased further to levels below the Cs_2Te threshold, the relative QE falls progressively to extremely low levels ($<10^{-6}$), although the precise behavior is not consistent for all cathodes.

B. Photocathode deposition and performance

The synthesis of high-quality Cs-Te cathodes and the difficulties therein is a topic that is well covered by published photocathode literature. The challenges in the consistent manufacture of high-brightness photocathodes for particle accelerators that meet the required performance specifications are widely recognized [3,33,51,52]. Furthermore, Rutherford backscattering spectroscopic measurements have shown that copper reacts with a Cs_2Te overlayer creating a hybrid compound [53] with electrical properties that differ from those of pure Cs_2Te. Molybdenum is more stable and is accepted as being a better substrate for a Cs_2Te photocathode. However, one of the primary drivers for this work was to gain a deeper understanding of the performance of photocathodes used at CERN for the CLIC [13], CLEAR [14], and AWAKE [15] projects, so no changes were made to the CERN photocathode deposition process which uses a copper puck. The choice of copper as the substrate was made decades ago for the CLIC Test Facilities (CTF) since copper exhibits good rf properties, which is particularly important for high gradients in the range of 120 MV/m. Additionally, XPS analyses performed on thick (tens of nm) Cs-Sb [39] and Cs-K-Sb [38] photocathodes deposited on copper substrates showed no traces of copper on the surface. Furthermore, when SwissFEL compared the use of CsTe on copper to pure copper photocathodes, they found that the CsTe behaved as expected [52].

On visual inspection, the Cs-Te photocathodes received at Daresbury Laboratory exhibited a significant degree of variability, as can be seen in Fig. 3. The deposition data from CERN shown in Fig. 1 and summarized in Table I also show that there were substantial differences in the elemental deposition rates and total film thicknesses at the time of manufacture for each photocathode. This translates into visible differences under normal laboratory illumination conditions and ultimately performance differences when illuminated for photoemission. This variability was evident in the analysis of the XPS and MTE datasets.

The behavior of these photocathodes at wavelengths beyond the expected Cs_2Te emission threshold is of interest. An explanation for this behavior is based on the XPS data presented in Sec. VI and in Appendixes C to E which show the presence of multiple photoemitting chemical species on these photocathode surfaces, specifically Te, Cs_2Te, Cs, and Cs_zO.

Te has a work function of 4.95 eV [54] and this energy is not reached until the illumination wavelength is below 250 nm. Consequently, the presence of elemental Te does not have a notable effect on photoemission performance. Furthermore, no elemental tellurium can be detected within the probing depth of the XPS technique. The P6 photocathode had a greater nominal thickness of Cs deposited in comparison to any of the other photocathodes, as shown in Table I, and our XPS measurements summarized in Table III show that no elemental Te was detected through the overlying Cs_2Te layer.

We assume the Cs_2Te work function is 3.5 eV [2,33,50] which equates to an emission threshold at 350 nm. At room temperature, Cs and Te are known to form a family of stable Cs_xTe_y compounds with a range of crystal structures, and by extension, some variance in overall work function [55]. When the temperature is elevated, the Cs-Te system is known to exhibit an enhanced level of volatility with an even wider range of compounds formed and a strong affinity to react with oxygen and water [56,57].

The manufacture of a Cs_2Te photocathode inevitably leads to an excess of unreacted (elemental) Cs that affects the overall work function of the photoemissive surface [2,51]. The deposition data shown in Table I show an excess of Cs for all of the photocathodes in this study. Cs has a work function of 2.14 eV (580 nm) [54] and has a strong affinity for O_2 to form Cs_2O which has an even lower work function of around 1.4 eV for a thin Cs_2O layer on silver, falling to around 1.0 eV for a thick layer [57,58]. The work function reduction is strongly related to the level of oxygen exposure.

C. Analysis of the P5 cathode performance

To simplify our performance analysis of these photocathodes, we define the following specific ranges for illumination wavelength (λ) which are linked to the compound and element work functions discussed previously: (i) "UV" as the wavelength region covering the expected Cs_2Te spectral response range with photon energies between 5.0 and 3.5 eV ($\lambda < 350$ nm); (ii) "UV-blue" as

the wavelength region between the Cs_2Te threshold and visible with photon energies between 3.5 and 3.1 eV ($350 < \lambda < 400$ nm); (iii) "vis-blue" as the visible wavelength region to the Cs emission threshold with photon energies between 3.1 and 2.1 eV ($400 < \lambda < 580$ nm); and (iv) "vis-red" as the visible wavelength region beyond the Cs emission threshold with photon energies below 2.1 eV ($\lambda > 580$ nm).

The P5 cathode exhibited an initially high level of MTE which fell progressively as the illumination wavelength shifted over the UV range, although the k_BT threshold was not reached. Instead, our TEDC data around the threshold region exhibited a shoulder which we attribute to the presence of two photoemitting species with different workfunctions. As elemental Te has a high work function, this was not a contributing factor. We assign the photoemissive sources in this data as Cs_2Te (more loosely Cs_xTe_y [56]) and elemental Cs whose work functions are 3.5 and 2.14 eV, respectively. With the P5 cathode illuminated at close to 5.0 eV, the TESS detector was initially collecting electrons photoemitted from Cs_2Te with those from Cs possessing higher MTE and so appearing as a pedestal elevating the background in the photoemission footprint. The relative QE of the Cs emitter was around 3 orders of magnitude below the Cs_2Te, so it is likely that at the higher photon illumination energies, electrons emitted from Cs possessing the highest transverse energy component missed the detector altogether as the data acquisition was optimized for the dominant emitter, Cs_2Te. Around the Cs_2Te emission threshold, the vanishing Cs_2Te emission appeared clearly as a low MTE footprint superimposed on the higher MTE elevated background arising from Cs photoemission, however, the TESS detector settings applied over the UV range were maintained as the photon energy was progressively reduced through the UV-blue range.

The significant step at 3.2 eV (386 nm) in the UV-blue range occurred because the TESS detector settings were reoptimized and the gain increased, focusing now only on the weaker emission from Cs, and to some extent the Cs oxides (Cs_zO). Repeating the previous argument: As the illumination energy was shifted through the "vis-blue" and "vis-red" ranges, TESS now measured emission predominantly from the Cs. In addition to emission from Cs, we cannot rule out contributions from Cs_zO components, from which the photoemitted electron MTE will be even larger than that from the Cs due to Cs_zO possessing an even lower work function.

Our TEDC data show that the MTE of cathode P5 progressively decreases until reaching the thermal floor at an emission threshold of 2.0 eV (616 nm), only slightly beyond the expected Cs work function of 2.14 eV [54]. Additionally, we observed a significant decrease in the relative QE as the illumination energy approaches and crosses the Cs work function threshold. On reaching the

thermal floor at this longer wavelength, the emission is now more than 7 orders of magnitude below that of Cs_2Te at 4.66 eV (266 nm).

Although we do not have the XPS data for the P5 cathode as it was dropped in the TESS following TEDC acquisition, the deposition data show that the P5 was likely to be the most Cs-rich of all of the photocathodes, with a significant excess of Cs recorded at CERN during manufacture. By extension, a substantial amount of elemental Cs and Cs_zO is expected on the P5 surface, resulting in the emission threshold falling at the longest wavelength in the vis-red region.

D. Analysis of the P6, P7, and P8 photocathodes

The photoemission behavior of the P6, P7, and P8 cathodes are broadly similar to that explored in detail for the P5 cathode, although the increase in MTE when illuminated outside of the UV region is less significant, and our data are more continuous as the TESS detector was not adjusted in the way it was for the P5 cathode. The P6, P7, and P8 cathodes either reached the thermal floor or ceased to emit measurable TEDC in the vis-blue region, differing from the Cs-rich P5 cathode which reached the vis-red. Our data for the P8 cathode show that it reached the k_BT thermal floor at 2.9 eV (426 nm), and the P7 came very close to the floor at 3.2 eV (386 nm).

We took TEDC data for these cathodes with cryogenic cooling to $\sim$190 K while illuminated through the UV-blue and vis-blue regimes, and one notable difference is that the MTE measured for these cathodes was increased by cooling, and the spectral response increased for the P6 cathode. We attribute this to the affinity of Cs for O_2 which was enhanced by cryopumping when the photocathodes were cooled [58]. The room temperature TEDC was recorded first, and then the cryogenic TEDC, so we link this change in surface chemistry to the cooling process which we believe increased the fraction of Cs_zO on the photoemissive surfaces of these cathodes.

The difference in relative QE over the Cs_2Te spectral response range (236 nm–350 nm) is more than 3 orders of magnitude, with a further 3 or more orders of magnitude from the Cs_2Te threshold to the point where detectable photoemission ceased. We have identified in previous publications [26,59] that the practical dynamic range of the TESS detector is less than 2 orders of magnitude. Therefore, it is not possible to illuminate a photocathode at a short wavelength (e.g., 4.66 eV/266 nm) while simultaneously collecting and resolving both the dominant high-level photoemission from Cs_2Te and the low-level contribution from Cs and Cs_zO. Of course, the relative contribution of Cs and Cs_zO to the overall photoemission footprint is small, as evidenced by the XPS and relative QE data, but they are present nonetheless and photoemit with high transverse energy components.

Cs is highly reactive with a strong affinity for oxygen and oxygen-containing compounds [56,57]. We attribute the oxygen detected on the P6 and P7 cathodes to this, but the lack of oxygen in the P8 XPS data implies that this contamination did not occur during transportation in the vacuum suitcase. The oxygen must have been present at the time of photocathode manufacture, most likely in the form of water vapor at a low partial pressure in the deposition system at CERN. The order of photocathode manufacture was P7, P5, P6, and finally P8. As can be seen from the XPS data summarized in Appendixes C to E and detailed in Tables V, VI, and VII, the measured oxygen concentration fell as the manufacturing process progressed, suggesting that the deposition of cesium served to fix any residual oxygen-containing species in the deposition vacuum system and effectively remove this. Consequently, the optimal deposition conditions existed at the time of the P8 manufacture, and hence there was no detectable oxygen.

Reference [60] (and references therein) explores the presence of a low QE photoemission shoulder at visible wavelengths which vanished with the application of additional Cs and heating. This behavior is attributed to the formation of Cs_5Te_3 and metallic Cs and caused nonmonotonic behavior when the cathode was cooled. Our data also show nonmonotonic behavior, particularly for the P6 cathode, although our XPS data do not allow us to specifically link this to the presence of Cs_5Te_3. As the cathodes in this work were deposited at room temperature and were not subjected to any subsequent heating/ annealing, and on the basis of our XPS data, we believe that the nonmonotonic behavior and extended spectral response for these cathodes are due to the presence of Cs_xTe_y, Cs, and Cs_zO compounds.

Recent work to characterize Cs_2Te photocathodes grown at Daresbury Laboratory has shown similar overall behaviors, with nonmonotonic MTE and detectable photoemission under illumination wavelengths far beyond the expected Cs_2Te emission threshold and the presence of multiple photoemitting species [61].

IX. SUMMARY AND CONCLUSIONS

A batch of four Cs-Te photocathodes (viz. Cathodes P5 → P8) produced at CERN was successfully transported in a custom-designed UHV suitcase to Daresbury Laboratory for characterization. The QE degradation during the transport was expected to be less than 1 percentage point based on the delivered gas dose of 1.6 L, and cathode P8 was found to have the highest QE of 2.9% at $\lambda = 265$ nm when measured at Daresbury at the end of the performance characterization process. Our photoemission analysis showed that all of the cathodes demonstrated an ability to emit photoelectrons at wavelengths beyond the Cs_2Te emission threshold due to the presence of additional photoemissive sources: Cs and Cs_zO confirmed by XPS.

This emission was enhanced through cryopumping when the cathodes were cooled, thereby increasing the fraction of Cs oxides on the cathode surface, and consequently, the QE measured at longer illumination wavelengths.

When illuminated at UV wavelengths, the presence of Cs and Cs oxides with their very low work functions leads to electron emission with very high levels of MTE, albeit representing a small fraction of the total photoemitted electron distribution as can be seen by the trend in the relative quantum efficiencies in Fig. 4. However, these photoelectrons will possess much larger transverse energy components than those emitted from Cs_2Te and have a large angular divergence from the point of emission on the photocathode surface and so are less likely to pass through the clear aperture within the accelerator vacuum system. This is perhaps most troublesome within a multicell rf gun where the clear aperture is generally small to maximize the on-axis electric field. The consequence will be the loss of electrons to the cavity walls, heat loading the cavity and driving electron-stimulated desorption which is detrimental to the photocathode lifetime and performance, and also to cavity performance.

It is debatable as to which was the "best" photocathode in this study. The XPS data imply that P8 was the best from a purely composition and contaminant perspective, but the spectral response of P7 is the most "conventional" and is superior to that of P8. It is unfortunate that the XPS data we took for P5 have no value due to its exposure to air when recovering it from the TESS, as this would most likely have demonstrated a high level of elemental Cs and Cs_zO. Only the P5 and P8 cathodes reached the thermal floor.

In closing, this work has demonstrated the success of our vacuum suitcase for the transportation of sensitive photocathodes over long distances. It has also highlighted the importance of controlling the nature of all photoemitting sources on a photocathode surface. A consistent approach during deposition is essential to achieve the ideal elemental ratio during Cs_2Te growth and so achieve optimum performance and spectral response.

APPENDIX A: TRANSPORT SUITCASE AND TRANSFER ASSEMBLY
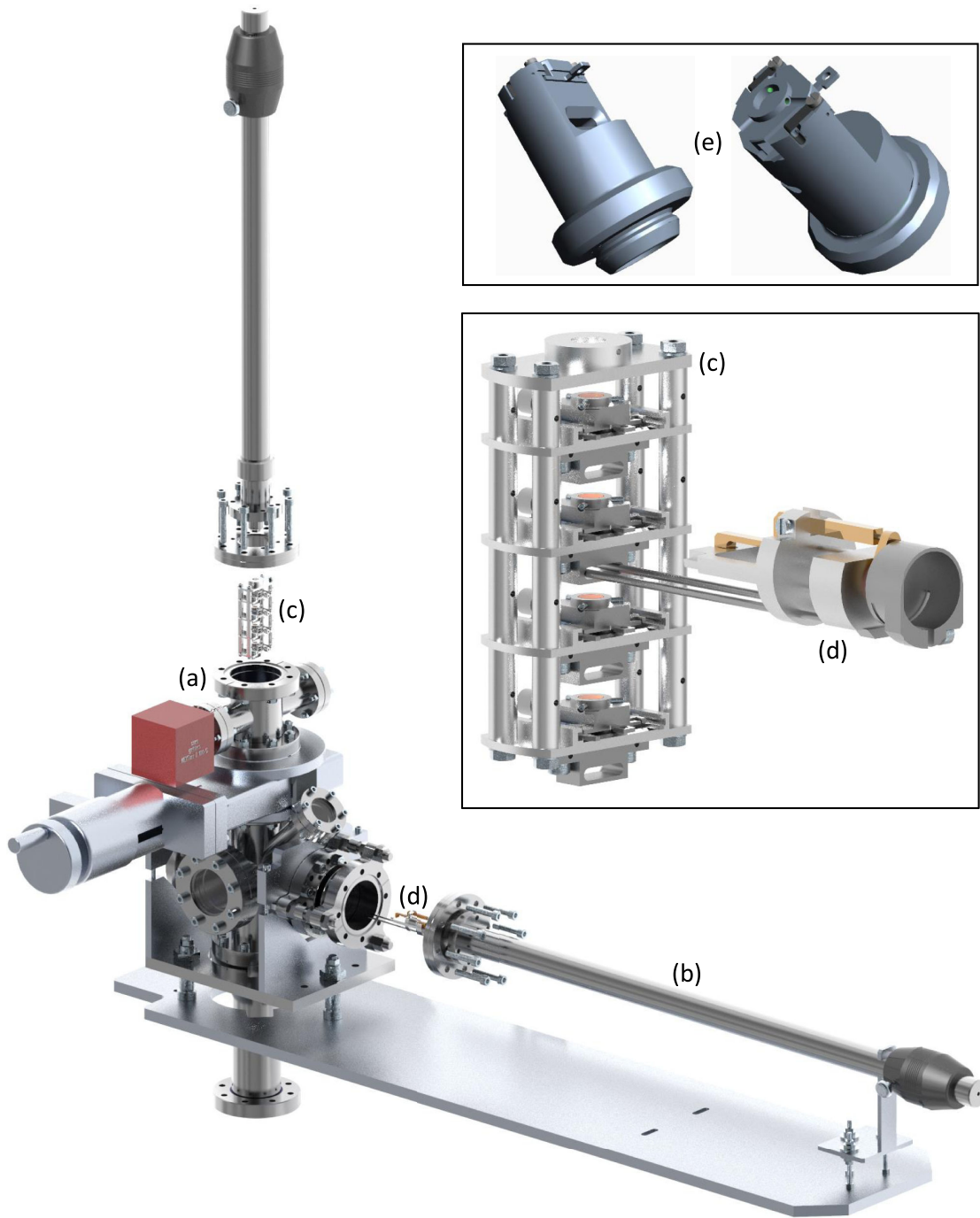
FIG. 5.　Computer-aided renderings showing an exploded view of the UHV suitcase (a) and the cathode sample transfer-arm assembly (b). The *lower detail inset* shows the cathode magazine (c) loaded with four Omicron flag sample holders containing copper pucks, and the Omicron tong mechanism (d) used to move these sample holders. The *upper detail inset* shows the puck adapter (e) used in the CERN deposition system to provide a dock for the Omicron flag sample plates used by STFC.

APPENDIX B: STM SURFACE ROUGHNESS MEASUREMENTS
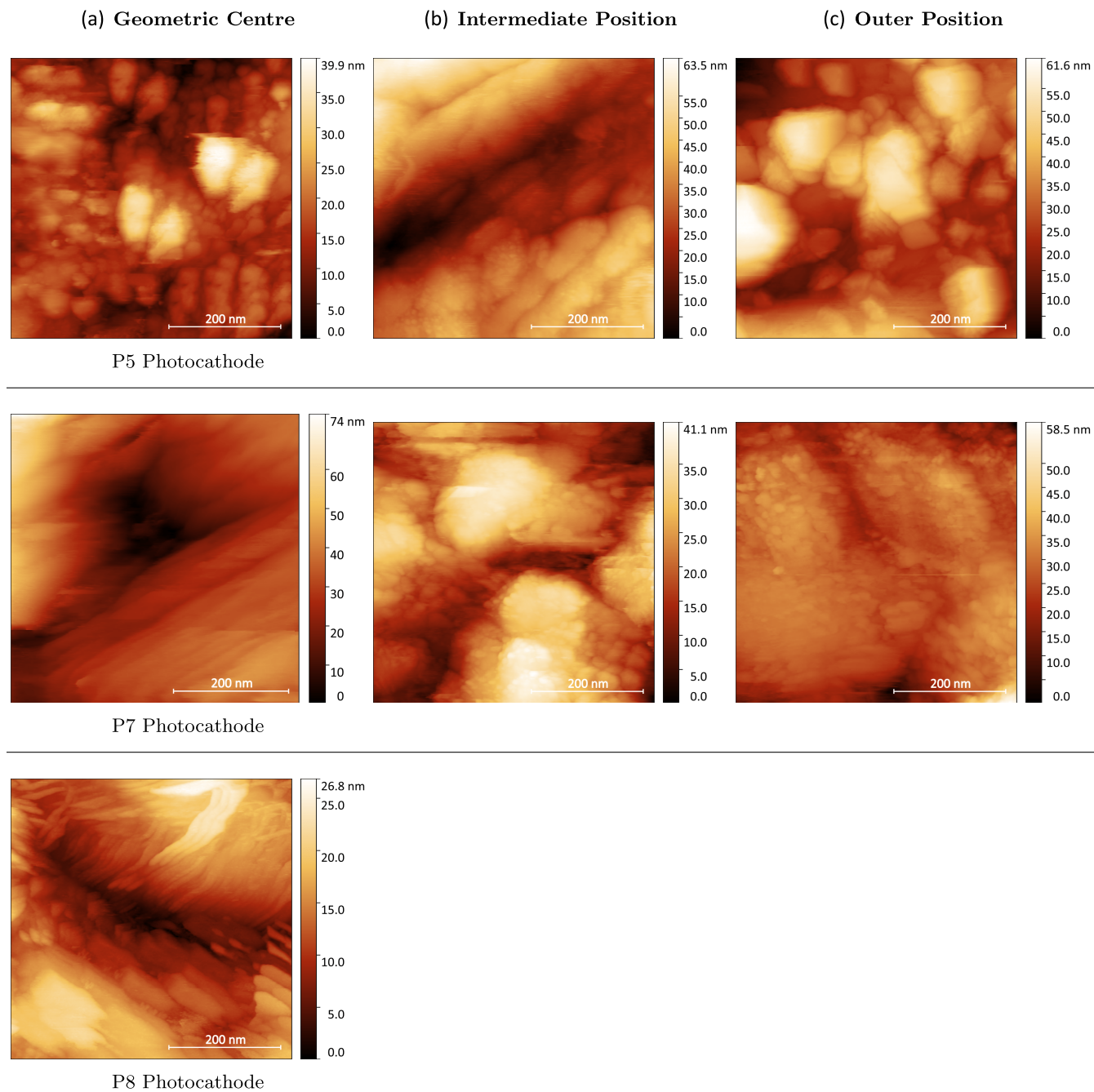
FIG. 6.   STM images of the photocathode surfaces taken over a 500 nm × 500 nm area, with column (a) measured at the geometric center, column (b) at the intermediate position with a radial displacement of ∼0.75 mm from the center, and column (c) at the outer position with a radial displacement of ∼1.50 mm from the center.

APPENDIX C: XPS SURFACE CHEMISTRY ANALYSIS FOR THE P6 CATHODE
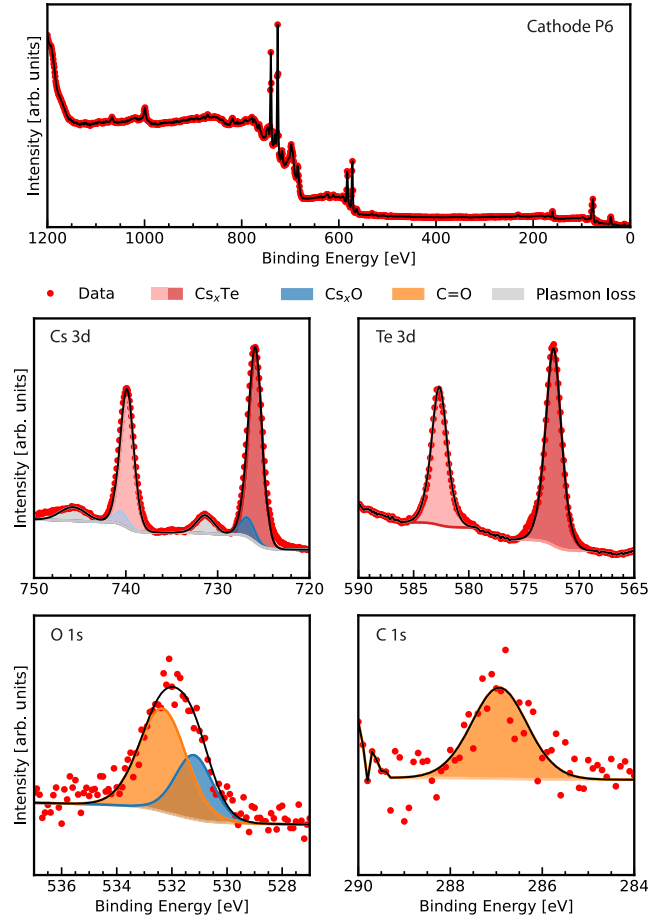
FIG. 7.　XPS surface chemistry with peak fitting using CASAXPS [46], NIST binding energies [47], and Scofield RSFs [48].

TABLE V.　P6 XPS elemental composition with bonding environments based on the data fitting shown in Fig. 7.

Region	Bonding environment	Fit peak position (eV)	Fit peak FWHM (eV)	Concentration (%)
Cs3d$^{5/2}$	Cs$_x$Te	725.9	1.7	24.8
3d$^{5/2}$	CsO	726.8	1.8	2.7
Cs3d$^{3/2}$	Cs$_x$Te	739.8	1.7	24.3
3d$^{3/2}$	CsO	740.5	1.8	2.5
Te 3d$^{5/2}$	Cs$_x$Te	572.3	1.7	17.7
3d$^{3/2}$	Cs$_x$Te	582.7	1.7	17.6
O 1s	CsO	531.2	1.6	2.1
	Organic	532.3	2.0	4.1
C 1s	Organic	286.9	1.4	4.2

APPENDIX D: XPS SURFACE CHEMISTRY ANALYSIS FOR THE P7 CATHODE
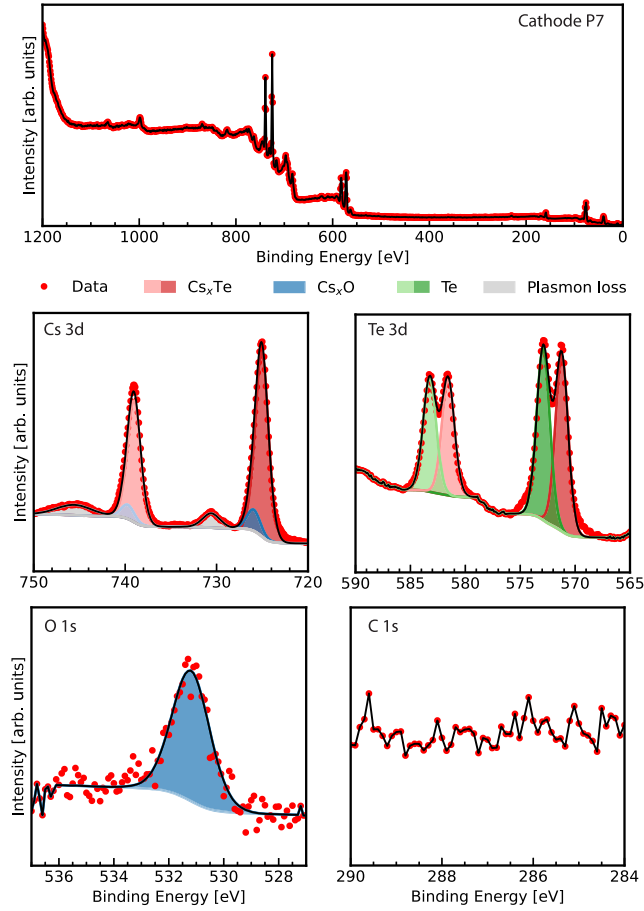
FIG. 8.   XPS surface chemistry with peak fitting using CasaXPS [46], NIST binding energies [47], and Scofield RSFs [48].

TABLE VI.   P7 XPS elemental composition with bonding environments based on the data fitting shown in Fig. 8.

Region	Bonding environment	Fit peak position (eV)	Fit peak FWHM (eV)	Concentration (%)
$Cs3d^{5/2}$	Cs_2Te	725.0	1.7	24.9
$3d^{5/2}$	CsO	726.0	1.8	2.9
$Cs3d^{3/2}$	Cs_2Te	739.0	1.7	24.1
$3d^{3/2}$	CsO	739.7	1.8	2.7
$Te\,3d^{5/2}$	Cs_2Te	571.2	1.4	10.8
$3d^{5/2}$	Te	572.9	1.4	10.8
$Te\,3d^{3/2}$	Cs_2Te	581.6	1.4	10.1
$3d^{3/2}$	Te	583.3	1.4	10.2
O 1s	CsO	531.2	1.6	3.5

APPENDIX E: XPS SURFACE CHEMISTRY ANALYSIS FOR THE P8 CATHODE
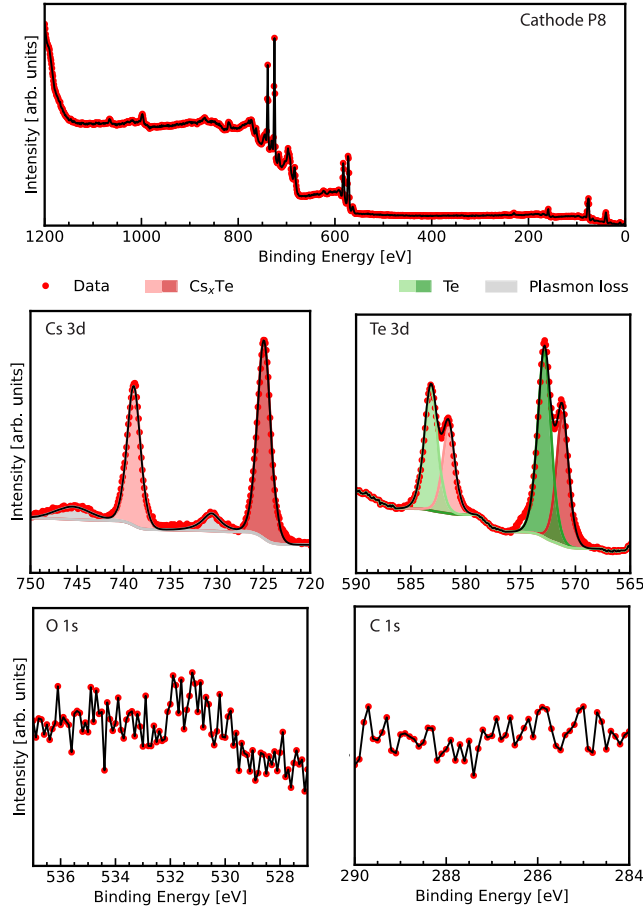
FIG. 9. XPS surface chemistry with peak fitting using CasaXPS [46], NIST binding energies [47], and Scofield RSFs [48].

TABLE VII. P8 XPS elemental composition with bonding environments based on the data fitting shown in Fig. 9.

Region	Bonding environment	Fit peak position (eV)	Fit peak FWHM (eV)	Concentration (%)
Cs3d$^{5/2}$	Cs$_2$Te	725.0	1.7	25.6
Cs3d$^{3/2}$	Cs$_2$Te	738.9	1.7	25.3
Te 3d$^{5/2}$	Cs$_2$Te	571.2	1.3	10.0
3d$^{5/2}$	Te	572.8	1.4	15.3
Te 3d$^{3/2}$	Cs$_2$Te	581.6	1.3	9.4
3d$^{3/2}$	Te	583.2	1.4	14.4

[1] K. L. Jensen, *Advances in Imaging and Electron Physics* (Elsevier Academic Press, San Diego, 2007), p. 149.

[2] R. A. Powell, W. E. Spicer, G. B. Fisher, and P. Gregory, Photoemission studies of cesium telluride, Phys. Rev. B **8,** 3987 (1973).

[3] A. di Bona, F. Sabary, S. Valeri, P. Michelato, D. Sertore, and G. Suberlucq, Auger and x-ray photoemission spectroscopy study on Cs_2Te photocathodes, J. Appl. Phys. **80,** 3024 (1996).

[4] S. H. Kong, J. Kinross-Wright, D. C. Nguyen, and R. L. Shieffield, Cesium telluride photocathodes, J. Appl. Phys. **77,** 6031 (1995).

[5] G. Loisch and Y. Chen et al., Direct measurement of photocathode time response in a high-brightness photoinjector, Appl. Phys. Lett. **120,** 104102 (2022).

[6] A. Aryshev, Y. Honda, K. Lekomtsev, M. Shevelev, N. Terunuma, and J. Urakawa, Cs_2Te photocathode response time measurements and femtosecond comb electron beam generation as a milestone towards pre-bunched THz FEL realization, in *Proceedings of the 7th International Particle Accelerator Conference, Busan, Korea* (JACoW, Geneva, Switzerland, 2016), THPOW007.

[7] D. H. Dowell and J. F. Schmerge, Quantum efficiency and thermal emittance of metal photocathodes, Phys. Rev. ST Accel. Beams **12,** 074201 (2009).

[8] M. C. Divall, E. Prat, S. Bettoni, C. Vicario, A. Trisorio, T. Schietinger, and C. P. Hauri, Intrinsic emittance reduction of copper cathodes by laser wavelength tuning in an rf photoinjector, Phys. Rev. ST Accel. Beams **18,** 033401 (2015).

[9] C. Gulliford et al., Demonstration of low emittance in the Cornell energy recovery linac injector prototype, Phys. Rev. ST Accel. Beams **16,** 073401 (2013).

[10] E. Prat et al., Generation and characterization of intense ultralow-emittance electron beams for compact x-ray free-electron lasers, Phys. Rev. Lett. **123,** 234801 (2019).

[11] Y. Ding et al., Measurements and simulations of ultralow emittance and ultrashort electron beams in the Linac Coherent Light Source, Phys. Rev. Lett. **102,** 254801 (2009).

[12] C. A. Lindstrøm and M. Thévenet, Emittance preservation in advanced accelerators, J. Instrum. **17,** P05016 (2022).

[13] P. Roloff, CLIC Conceptual Design Report, CERN Report No. CERN-2012-005, 2018, https://cds.cern.ch/record/2652257/files/ESUInput_CLICPhysics_final.pdf.

[14] K. N. Sjobak et al., Status of the CLEAR Electron Beam User Facility at CERN, in *Proceedings of the 10th International Particle Accelerator Conference, Melbourne, Australia* (JACoW, Geneva, Switzerland, 2019), MOPTS054.

[15] E. Adli et al., Acceleration of electrons in the plasma wakefield of a proton bunch, Nature (London) **561,** 363 (2018).

[16] E. Gschwendtner et al., The AWAKE run 2 programme and beyond, Symmetry **14,** 1680 (2022).

[17] R. Ramjiawan, V. Bencini, P. N. Burrows, and F. M. Velotti, Design of the proton and electron transfer lines for AWAKE Run 2c, Nucl. Instrum. Methods Phys. Res., Sect. A **1049,** 168094 (2023).

[18] P. Michelato, C. Gesmundo, and D. Sertore, High quantum efficiency photocathodes preparation system for the TTF Injector II, INFN Technical Report No. INFN/TC–00/19, 2000.

[19] D. Sertore, P. Michelato, L. Monaco, P. Manini, and F. Siviero, Use of non–evaporable getter pumps to ensure long term performances of high quantum efficiency photocathodes, J. Vac. Sci. Technol. A **32,** 031602 (2014).

[20] S. Mohanty et al., Development and test results of multi-alkali antimonide photocathodes in the high gradient RF gun at PITZ, in *Proceedings of the 40th International Free Electron Laser Conference, Trieste, Italy* (JACoW, Geneva, Switzerland, 2022), TUP04.

[21] F. Sannibale et al., Advanced photoinjector experiment photogun commissioning results, Phys. Rev. ST Accel. Beams **15,** 103501 (2012).

[22] D. Filippetto, H. Qian, and F. Sannibale, Cesium telluride cathodes for the next generation of high–average current high-brightness photoinjectors, Appl. Phys. Lett. **107,** 042104 (2015).

[23] B. L. Militsyn, I. Burrows, R. J. Cash, B. D. Fell, L. B. Jones, J. W. McKenzie, K. J. Middleman, H. E. Scheibler, and A. S. Terekhov, First results from the III-V Photocathode Preparation Facility for the Alice ERL Photoinjector, in *Proceedings of the International Particle Accelerator Conference, Kyoto, Japan, 2010* (ICR, Kyoto, 2010), TUPE095.

[24] F. Jackson et al., The status of the Alice R&D Facility at STFC Daresbury Laboratory, in *Proceedings of the 2nd International Particle Accelerator Conference, IPAC-2011, San Sebastián, Spain* (EPS-AG, Spain, 2011), TUODA03.

[25] T. C. Q. Noakes, B. L. Militsyn, R. Valizadeh, K. J. Middleman, A. N. Hannah, and L. B. Jones, Commissioning of the SAPI for operation with metal photocathodes, EuCARD-2, Report No. CERN-ACC-2014-0039, 2014.

[26] L. B. Jones, D. P. Juarez-Lopez, H. E. Scheibler, A. S. Terekhov, B. L. Militsyn, C. P. Welsch, and T. C. Q. Noakes, The measurement of photocathode transverse energy distribution curves (TEDCs) using the transverse energy spread spectrometer (TESS) experimental system, Rev. Sci. Instrum. **93,** 113314 (2022).

[27] H. M. Churn, C. Benjamin, L. B. Jones, and T. C. Q. Noakes, The alkali-metal Photocathode Preparation Facility at Daresbury Laboratory: First caesium telluride deposition results, in *Proceedings of the 13th International Particle Accelerator Conference, Bangkok, Thailand* (JACoW, Geneva, Switzerland, 2022), THPOPT044.

[28] J. A. Clarke et al., CLARA Conceptual Design Report (2013).

[29] L. Whitmore, R. I. Mackay, M. van Herk, J. K. Jones, and R. M. Jones, Focused VHEE (Very High Energy Electron) beams and dose delivery for radiotherapy applications, Sci. Rep. **11,** 14013 (2021).

[30] Q. Gao et al., Observation of high transformer ratio of shaped bunch generated by an emittance-exchange beam line, Phys. Rev. Lett. **120,** 114801 (2018).

[31] L. B. Jones and D. P. Juarez-Lopez et al., Report on the performance characterisation of caesium telluride and caesium potassium antimonide photocathodes manufactured at CERN, STFC DL Report No. ASTEC-AP-2020-001, 2021, https://epubs.stfc.ac.uk/manifestation/53568912/CERN+2020+ASTeC+Report.pdf.

[32] Omicron Spare Parts Catalogue SPM, v.2.4 (5 July 2019) pg. 3; Part No. S220601-S.

[33] M. Gaowei, J. Sinsheimer, D. Strom, J. Xie, J. Cen, J. Walsh, E. Muller, and J. Smedley, Codeposition of ultra-smooth and high quantum efficiency cesium telluride photocathodes, Phys. Rev. ST Accel. Beams **22**, 073401 (2019).

[34] G. Suberlucq, Technological challenges for High Brightness Photo-injectors, in *Proceedings of the 9th European Particle Accelerator Conference, Lucerne, Switzerland* (2004), p. 64.

[35] J. Teichert, R. Xiang, G. Suberlucq, and J. Verschuur, Report on photocathodes, CARE Note-2004-033-PHIN, 2004.

[36] C. Ghosh and B. P. Varma, Preparation and study of properties of a few alkali antimonide photocathodes, J. Appl. Phys. **49**, 4549 (1978).

[37] E. Chevallay, Experimental results at the CERN. Photo-emission Laboratory with co-deposition photocathodes in the frame of the CLIC studies, CERN CTF3 Note No. 104, 2012.

[38] H. Panuganti, E. Chevallay, V. Fedosseev, and M. Himmerlich, Synthesis, surface chemical analysis, lifetime studies and degradation mechanisms of Cs-K-Sb photocathodes, Nucl. Instrum. Methods Phys. Res., Sect. A **986**, 164724 (2021).

[39] I. Martini, Characterization of Cs-Sb cathodes for high charge RF photoinjectors, Doctoral dissertation, Politechnico di Milano, Italy, 2015.

[40] Omicron Spare Parts Catalogue System, v.1.0 (27 June 2019), pg. 10; Part No. PN01887-S.

[41] P. Michelato, L. Monaco, C. Pagani, D. Sertore, and J. Smedley, Cs_2Te photocathodes robustness studies, in *Proceedings of the 11th European Particle Accelerator Conference, Genoa, Italy* (EPSAG, Geneva, 2008), MOPC075.

[42] L. B. Jones, H. E. Scheibler, D. V. Gorshkov, A. S. Terekhov, B. L. Militsyn, and T. C. Q. Noakes, Evolution of the transverse and longitudinal energy distributions of electrons emitted from a GaAsP photocathode as a function of its degradation state, J Appl. Phys. **121**, 225703 (2017).

[43] K. Flöttmann, Note on the thermal emittance of electrons emitted by cesium telluride photo cathodes, TESLA FEL-Report No. 1997-01, 1997.

[44] D. Nečas and P. Klapetec, Gwyddion: An open-source software for SPM data analysis, Central Eur. J. Phys. **10**, 181 (2012).

[45] P. Ruffieux, P. Schwaller, O. Gröning, L. Schlapbach, P. Gröning, Q. C. Herd, D. Funnemann, and J. Westermann, Experimental determination of the transmission factor for the Omicron EA125 electron analyzer, Rev. Sci. Instrum. **71**, 3634 (2000).

[46] N. Fairley *et al.*, Systematic and collaborative approach to problem solving using x-ray photoelectron spectroscopy, Appl. Surf. Sci. Adv. **5**, 100112 (2021).

[47] A. V. Naumkin, A. Kraut-Vass, S. W. Gaarenstroom, and C. J. Powell, NIST X-ray Photoelectron Spectroscopy Database (2000), 10.18434/T4T88K.

[48] J. H. Scofield, Hartree-Slater subshell photoionization cross-sections at 1254 and 1487 eV, J. Electron Spectrosc. Relat. Phenom. **8**, 129 (1976).

[49] S. Lederer *et al.*, XPS studies of Cs_2Te photocathodes, in *Proceedings of Free Electron Laser Workshop, Novosi-birsk, Russia* (JACoW, Geneva, Swotzerland, 2007), WEPPH048.

[50] M. Gaowei (private communication).

[51] R. A. Loch, Cesium-telluride and magnesium for high quality photocathodes, Master's thesis, University of Twente, 2005.

[52] E. Prat, S. Bettoni, H. H. Braun, R. Ganter, and T. Schietinger, Measurements of copper and cesium telluride cathodes in a radio-frequency photoinjector, Phys. Rev. ST Accel. Beams **18**, 043401 (2015).

[53] R. Xiang *et al.*, Cs_2Te normal conducting photocathodes in the superconducting rf, Phys. Rev. ST Accel. Beams **13**, 043501 (2010).

[54] H. B. Michaelson, The work function of the elements and its periodicity, J. Appl. Phys. **48**, 4729 (1977).

[55] G. Prins and E. H. P. Cordfunke, Compounds in the system Cs-Te at room temperature, J. Less-Common Met. **104**, L1 (1984).

[56] J. McFarlane and J. C. LeBlanc, Fission-product tellurium and cesium telluride chemistry revisited, Atomic energy of Canada Ltd., Whiteshell Laboratories Reports No. AECL-11333, COG-95-276-I, 1996.

[57] A. Band, A. Albu-Yaron, T. Livneh, H. Cohen, Y. Feldman, L. Shimon, R. Popovitz-Biro, V. Lyahovitskaya, and R. Tenne, Characterization of oxides of cesium, J. Phys. Chem. B **108**, 12360 (2004).

[58] J. J. Uebbing and L. W. James, Behavior of cesium oxide as a low workfunction coating, J. Appl. Phys. **41**, 4505 (1970).

[59] L. B. Jones, H. E. Scheibler, S. N. Kosolobov, A. S. Terekhov, B. L. Militsyn, and T. C. Q. Noakes, Non–monotonic behaviour in the mean transverse energy of electrons emitted from a reflection–mode p-GaAs(Cs,O) photocathode during its QE degradation through oxygen exposure, J. Phys. D **54**, 205301 (2021).

[60] C. M. Pierce, J. K. Bae, A. Galdi, L. Cultrera, I. Bazarov, and J. Maxson, Beam brightness from Cs–Te near the photoemission threshold, Appl. Phys. Lett. **118**, 124101 (2021).

[61] H. M. Churn, L. B. Jones, and T. C. Q. Noakes, Mean transverse energy and degradation measurements on a Cs_2Te photocathode, in *Proceedings of the 14th International Particle Accelerator Conference, Venice, Italy* (JACoW, Geneva, Switzerland, 2023), TUPA030.